Factors Leading to the Break Up of Marine Stratocumulus: A Lagrangian Perspective using the A-Train Satellites

Ryan Eastman, Robert Wood

University of Washington

Department of Atmospheric Sciences

February 2015

Ryan Eastman

Box 351640

Seattle WA 98195

rmeast@atmos.washington.edu

Abstract

Over 66,000 cloud scenes are sampled using CloudSat, CALIPSO, MODIS, and AMSR/E. Samples are taken in stratocumulus decks in the NE and SE Pacific, SE Atlantic, and E Indian oceans. Horizontal wind fields at 925mb from ERA-interim reanalyses are used to compute a 24-hour, 2-D, forwards, boundary layer trajectory for each sample. Cloud properties are sampled at 12- and 24-hours along the trajectories, allowing for a direct assessment of the evolution of stratocumulus given a variety of initial conditions. Analyses are done for seasonal anomalies for quantities of total cloud cover, liquid water path, and cloud droplet concentration with satellite zenith angle biases removed. When averaged, all three quantities show a consistent near-linear relationship between initial anomalies and their 24-hour Lagrangian change. This relationship is used to compare the actual change in each sample with the expected change (for the population as a whole), allowing for a comparison that is not influenced by differences in initial values.

Results tend to support previous modeling, theoretical, and observational studies, showing that stratocumulus in deep boundary layers or under weaker inversions is prone to breakup. Results are not entirely consistent between regions. Precipitation shows a more complex, less statistically significant, and regionally variable relationship with cloud breakup. Clouds in shallow precipitating boundary layers appear more persistent than those in deep precipitating boundary layers. Areally averaged liquid water path decreases more rapidly for precipitating clouds and in deep boundary layers. Droplet concentration in shallow boundary layers decreases more rapidly with increased precipitation. Droplet concentration decreases less slowly in shallow boundary layers than in deep boundary layers, where droplet concentration shows a consistent decline regardless of precipitation or inversion strength.

1. Introduction

Subtropical marine stratocumulus (Sc) clouds cool Earth's climate significantly. Sc clouds radiate at temperatures nearly as warm as the sea surface, while they reflect much of the abundant sunlight in the subtropics (Hartmann and Short, 1980). The massive extent of subtropical Sc decks combined with their strong cooling influence makes it essential that we understand the nature of their formation, mesoscale variability, physical processes, and eventual dissipation (Wood, 2012), dissipation being our focus here.

Stratocumulus clouds in subtropical decks undergo a life cycle lasting several days. Bretherton and Wyant (1997) explain key aspects of the Planetary Boundary Layer (PBL) structure and consequences for cloud evolution using a mixed layer model. Persistent subtropical high-pressure systems direct warm air westward from the major continents over the relatively cool ocean. Marine Sc forms in the shallow, cool boundary layer that forms immediately offshore. Cloud tops emit longwave radiation upward, cooling the air at the cloud top, and driving overturning of the entire boundary layer. This boundary layer is characterized as 'coupled' since the radiatively driven circulation spans from cloud top to the sea surface. As the Sc is advected farther offshore and equatorward, entrainment of warm dry air at the cloud top combines with increased latent heating from warming SST's to deepen the boundary layer. Eventually the boundary layer is sufficiently deep to prevent the negatively buoyant parcels at the cloud top from reaching the surface, creating a cloud layer that is 'decoupled' from the sea surface. The "mixed-layer" beneath the Sc-containing layer continues to moisten and cumulus (Cu) clouds eventually form atop the mixed-layer, protruding into the Sc deck. The Sc deck eventually breaks up and is replaced by the underlying Cu. There is a pronounced diurnal cycle within this system favoring coupled boundary layers and more extensive cloud cover at night.

Prior studies show that numerous processes may act to prolong or shorten the transition from Sc to Cu. Sc amount in the NE Pacific was shown by Klein et al. (1995) to be dependent upon sea surface and upper air temperature 24-30 hours prior to cloud observation. Using a large-eddy simulation, Sandu and Stevens (2011) show that the pace of the Sc-Cu transition is primarily dictated by the strength of the temperature inversion at the beginning of the process, although they did not explore the range of phase space that exists in nature. Their simulation also suggests that precipitation and increased downwelling IR can quicken the Sc-Cu transition. Xiao et al. (2011), also using a large-eddy simulation, conclude that boundary layer decoupling due to surface evaporation is an important factor in Sc breakup. Wood and Bretherton (2004) use satellite data to show that strong entrainment is associated with deeper boundary layers, and that deeper boundary layers are far more likely to be decoupled. Wood and Hartmann (2006) also use satellite data to show that boundary layer depth plays a significant role in the physical and radiative properties of marine Sc. Zhou et al. (2015) use field data from the MAGIC campaign over the NE Pacific to show that Sc breakup occurs downwind of decoupling, and suggest that the primary driver of decoupling is dry air entrainment at the top of the cloud layer, while precipitation processes and surface latent heating were less impactful. Myers and Norris (2013) use satellite cloud data and reanalyses to show that stronger inversions lead to reduced entrainment and persistent clouds, and that increased large-scale subsidence compresses the boundary layer, leading to fewer, thinner clouds.

Precipitation processes within Sc are complex and no consensus affect on cloud evolution has been proven, though much has been proposed and modeled. Stevens et al. (1998) suggest that precipitation, by reducing entrainment, could slow down the decoupling transition. The model developed by Bretherton and Wyant (1997) shows that drizzle acts as a stabilizing force

within the boundary layer, where condensing water vapor releases latent heat at cloud top and evaporating rain cools the sub-cloud layer. They conclude that rain promotes decoupling in Sc decks, a conclusion substantiated by Mechem and Kogan (2003) using a coupled Ocean-Atmosphere model. Stevens et al. (2005) and Comstock et al. (2005) use field data to show that precipitation may lead to increased cloud cover variability and the development of "pockets of open cells", however Burleyson and Yuter (in press) show that cloud changes were not sensitive to precipitation on 1-3 hour time scales.

Klein et al. (1995) concluded that the Lagrangian histories of Sc within the marine boundary layer must be accounted for in order to predict how the clouds will evolve. Pincus et al. (1997) and Sandu et al. (2010) have done successful Lagrangian studies using wind fields from model reanalysis and composited satellite cloud data. Here, we use A-train satellite data and environmental data from ECMWF reanalyses to follow individual samples within Sc decks over a 24-hour period. We group samples based on their initial conditions and directly compare cloud changes to see whether the aforementioned conditions are significant. We do this by tracking cloud evolution for over 60,000 individual samples from four prominent subtropical Sc decks.

2. Data and Methods

a. Determining regions of study with surface observations

Figure 1 shows a climatology using long-term average cloud amounts based on surface observations of stratocumulus clouds (Hahn and Warren, 2007). Sc are most prevalent in regions of large-scale subsidence in subtropical eastern ocean basins as well as in the midlatitude storm-track. The red boxes in Figure 1 show our regions of study. These boxes capture the Sc maxima

off the west coasts of the continents and much of the cloud-cover gradient offshore. Within these regions we follow individual cloud scenes in easterly (offshore) flow under subtropical high-pressure ridges. We cut the regions off at 30° latitude to reduce the influence of weather systems in the midlatitude westerlies, which would lead to noisier and more variable trajectories.

b. Calculating trajectories and meteorological data using ERA interim and ECMWF-AUX

We use the wind fields from the ERA-interim reanalysis (Dee et al., 2011) dataset to produce ~66,000 individual trajectories for all months during the years 2007 and 2008. Our 2-D forward trajectories are calculated using the same routine as in Bretherton et al. (2010, Figure 9c & 9d). From the ERA-interim we use the horizontal wind fields at 925mb, within the PBL, at a latitude-longitude resolution of 0.75 degrees. Each trajectory begins at a point along the CloudSat and CALIPSO track. Points are chosen randomly along the track, and must be at least 200km apart. Random spacing allows us to observe a continuum of spatial scales, but is not relevant to this current study. We only study westward-propagating trajectories to eliminate the influence of eastward moving weather systems.

We take an initial cloud sample using CloudSat, CALIPSO, MODIS (Aqua only), and AMSR/E within a 100km radius of the trajectory beginning. We then sample the same cloud systems at 12 and 24 hours, within a 100km radius, following advection along the trajectory. At 12 and 24 hours we only use MODIS and AMSR/E, since those instruments have wide viewing angles. Figure 2 shows an example trajectory, the mean winds, the radii sampled, the initial CloudSat/CALIPSO and Aqua tracks, and the MODIS swaths at 0, 12, and 24 hours.

Meteorological data from ECMWF are interpolated to the CloudSat/CALIPSO track and made available as the ECMWF-AUX dataset. We use this ECMWF auxiliary dataset to

calculate the lower tropospheric stability (LTS) for all of our initial samples. We define LTS as the difference in potential temperature between the surface and 700mb.

c. Determining precipitation with CloudSat

Precipitation data come from the CloudSat 2C RAIN-PROFILE product (Mitrescu et al., 2010; Lebsock & L'Ecuyer, 2011). CloudSat uses a 94 GHz nadir-looking Cloud Profiling Radar. The resolution is 1.7 km along-track and 1.4 km cross-track. Vertical resolution within each sounding is 500 meters.

The Rain-Profile product contains a 'precip_flag' variable for each radar shot typically used, which is set to 1 if the pixel is determined to be raining at the surface. We classify a 200km-long sample along the CloudSat track as "precipitating" if one or more pixels have a precip_flag value of 1, otherwise the sample is considered "not-precipitating". We calculate a precipitation frequency variable for each sample, which is the percentage of soundings within a 200km-long sample that has a precip_flag value of 1.

CloudSat also offers a 'rain_rate' variable, measuring the intensity of precipitation reaching the surface in mm per hour. We combine the rate and frequency to create a sample rain rate variable, which quantifies the mean rain falling over an entire 200km sample in mm $hour^{-1}$.

d. Determining cloud top height with CALIPSO

We use the Cloud-Aerosol Lidar and Infrared Pathfinder Satellite Observations (CALIPSO) Vertical Feature Mask product (VFM, Vaughan et al. 2004) to determine the mean cloud top height at the beginning of each trajectory. Though not always exactly the case, we assume CALIPSO samples directly overlap CloudSat samples. We restrict the data to the lowest

3 km only, where each sounding represents a 90 meter-long footprint separated by 330 meters. Each 200 km-long sample contains ~600 individual VFM soundings. For each sounding we assume that the highest "cloud" return within the lowest 3 km represents the cloud top. We assume that the cloud top height also represents the PBL depth since marine Sc cloud tops typically sit at the base of the inversion and the highest clouds in a trade Cu field reach the trade inversion.

Calculating PBL depth for entire samples is often more complex than for individual soundings since cloud tops may not be consistent throughout. In some cases the PBL depth is quite obvious, as in Figure 3a, while in others it is more challenging to discern as shown in Figure 3b. The red line indicates the PBL depth assigned to the samples in Figure 3a and Figure 3b. To determine the PBL depth for each sample, we use a frequency distribution of cloud top heights. The frequency distribution for the cloud top heights for Figure 3b is shown in Figure 3c. The distribution shows multiple peaks, indicating multiple cloud tops within the sample. Peaks within the distribution are considered relevant if they are at least 40% as large as the largest peak. The cloud top height for the sample is assigned to the highest altitude relevant peak. In the case of Figure 3c the largest peak is also the highest relevant peak, at around 1.9 km. If no clouds are present in the sample the boundary layer depth cannot be determined, though this occurs less than 5% of the time.

e. Cloud amount, anomalies, and zenith angle bias for MODIS cloud mask data

All MODIS data for this study come from the gridded MODIS level 3 dataset (Hubanks et al. 2008, Oreopoulous 2005). We only use MODIS data from the Aqua satellite (MYD08_D3), which flies as a part of the A-Train constellation. Cloud fraction data come from

the cloud mask product within the level 3 dataset. Day and night cloud fractions are available on a 1°x1° latitude/longitude grid. A 1°x1° grid box is included in a sample if its center falls within 100 km of a sampling point along a trajectory. To reduce the effects of geographic and seasonal biases when comparing cloud evolution we convert all MODIS cloud fractions to seasonal anomalies by subtracting the mean seasonal cloud amount. Mean seasonal amounts are calculated separately for day and night for each individual 1° x1° grid box using all available data from 2007-2008. Seasons are defined as December, January, February; March, April, May; June, July, August; and September, October, November.

In order to sample nearly all of Earth in a single day the MODIS sensor relies on a very wide viewing angle, with a maximum sensor zenith angle of ~67°. Maddux et al. (2010) shows a ~14% discrepancy in cloud fraction between scenes viewed at the highest sensor zenith angle and scenes viewed at nadir, with larger cloud fractions seen at a higher angle. The CloudSat and CALIPSO satellite tracks are offset from the Aqua satellite track by ~215 km at the equator. Consequently, our initial (0-hour) samples are always seen at ~19° by MODIS, but our 12- and 24-hour observations are usually seen at much wider angles. Without addressing the change in zenith angles between 0-hour and later observations, we would show an erroneous increase in cloud cover as we followed our trajectories.

Figure 4 shows how we quantify the zenith angle bias over our study regions defined in Figure 1. We limit this analysis just to our study regions because the zenith angle bias could look different in other regions where cloud thickness and vertical structure are different. We show separate curves for day and night. The vertical error bars are centered on the mean cloud fraction and show the standard error of the mean for seven zenith angle bins. Mean cloud fraction is shown for each 10° zenith angle bin (0°-10°, 10°-20°… 60°-67°). Curves are the

polynomial fits to the means. We assume the bias is 0% at nadir, and at 67° the bias is ~5.5% at night and ~13% during the day.

Nighttime zenith angle data were not available from MODIS, requiring us to estimate the sensor zenith angle based on distance from the satellite track. Figure 4 shows the actual daytime zenith angle bias in blue and the estimated bias in red, both for daytime only. The overlap of the red and blue curves shows that our estimated zenith angles match the reported angles very closely. Data for the black line (night) rely only on estimated zenith angles. The difference between the red/blue curves and the black curve shows that the zenith angle bias is markedly different between day and night. This may be due to differing sensors used by MODIS during day and night, and also due to higher cloud fraction at night. Overcast conditions are more common at night, and the zenith angle bias is nonexistent for 100% cloud cover, leading to less overall nighttime bias.

Every seasonal cloud cover anomaly we calculate has the zenith angle bias removed based on the sample's mean sensor zenith angle. An example of how the zenith angle bias could impact our results is shown by the red and blue X's on Figure 4. Red X's show the mean zenith angle at 24 hours for trajectories that had no precipitation at their beginning. The blue X's show the mean zenith angle at 24 hours for trajectories that did show precipitation at their beginning. The angles are different because precipitating trajectories tend to originate farther offshore and travel farther to the west, so they are sampled at a lower angle the following day. The difference between the two angles is 7°, overall biasing cloud fraction at 24 hours for non precipitating samples high by 0.9% during the night and 2.2% during the day, both significant in the context of our results.

f. Droplet concentration and high cloud filter from MODIS optical properties

Liquid water path (LWP) and cloud droplet effective radius (r_e) come from the cloud optical properties product within the MODIS level 3 dataset. These variables are only available during daytime. Both LWP and r_e display a zenith angle bias. For sensor zenith angles between 0° and 65°, LWP shows a bias at high angles of -0.01 kg/m^2, and r_e shows a bias at high angles of 1.2 μm. The mean value of LWP is ~0.085 kg/m^2, and the mean of r_e is ~16.7 μm. After removing the zenith angle biases, we use these two variables and the relationship in the following equation (Boers et al., 2006; Bennartz, 2007) to estimate effective concentration (N_{eff}) specifically for clouds in the marine boundary layer:

Equation 1:
$$N_{eff} = \sqrt{2} B^3 \Gamma_{eff}^{1/2} \frac{LWP^{1/2}}{r_e(h)^3}$$

We then calculate droplet concentration with the relationship: $N_d = N_{eff}/k$, with k assumed to be to 0.8 for marine stratiform clouds (Martin et al. 1994, Wood 2000).

Similar to the MODIS cloud fraction data, we convert N_d values to seasonal anomalies in order to minimize any effects of geographical and seasonal variation.

We also use daytime cloud cover data from the MODIS L3 optical properties dataset to filter for high and middle cloud cover. The optical properties dataset provides a measure of ice cloud cover, unknown cloud cover, liquid cloud cover, and single-layer liquid cloud cover. For each trajectory we consider cloud observations to be free of interfering clouds if the measure of single-layer liquid cloud is equal to total liquid cloud, if the unknown cloud cover is equal to zero, and if the ice cloud cover is equal to zero. This filter is applied for all trajectories during daytime, so 24-hour trajectories beginning at night are filtered once during the day, while 24-

hour trajectories beginning during the day are filtered at their beginning and again at their end. Results have been processed with and without the filter and the vast majority of our figures were qualitatively unaffected by interfering clouds. Figures are labeled if they use filtered results.

g. LWP using AMSR - E

The Advanced Microwave Scanning Radiometer – EOS (AMSR-E) provides a separate measure of LWP for day and night (Wentz & Meissner, 2004), unlike the daytime-only MODIS LWP. The AMSR-E instrument is a passive-microwave radiometer carried aboard the Aqua satellite along with MODIS, providing concurrent sampling of clouds and cloud water content. The AMSR-E measures brightness temperatures at 6.925, 10.65, 18.7, 23.8, 36.5, and 89.0 GHz. The instrument has a swath width of 1450km, corresponding to a maximum sensor zenith angle of ~46°. We performed a zenith angle test for the AMSR-E LWP data in the same way as the MODIS data described above in section 2e, but did not find a significant zenith angle bias. AMSR-E level 3 data are averaged to match the 1°x1° grid of the level 3 MODIS data. After averaging, our sampling routines are identical for AMSR-E and MODIS.

Once again, to ensure that there are no geographic or seasonal biases in the LWP data we use a climatology of LWP from 2007-2008 to determine seasonal day and night LWP anomalies.

h. Bias due to differing initial distributions

The purpose of this work is to find environmental factors that would alter the evolution of otherwise identical starting scenes. One of our goals is to show how precipitation affects the evolution of stratocumulus. However, when grouping trajectories by whether or not there is precipitation (or virtually anything else), those two groups are unlikely to have identical mean

characteristics at their beginning (ie, they will have different starting mean cloud amounts). Figure 5 shows the relative frequency of initial cloud cover anomalies for precipitating and dry (non-precipitating) trajectories. It shows that precipitating trajectories tend to begin with more strongly positive cloud cover anomalies.

Figure 6 shows the relationship between mean starting cloud cover anomaly and mean delta cloud cover anomaly (ΔCCA) for our trajectories (blue line for 24-hours, green for 12). The slopes of the blue and green lines are both between 0 and -1. A slope of 0 would occur if ending anomalies were equal to beginning anomalies, while a slope of -1 would occur if ending anomalies were completely random relative to beginning anomalies. The slopes of the blue and green lines indicate that cloud cover anomalies tend to persist in time, but that there is a decorrelation over time, which is influenced by a wide variety of processes. Figure 6 suggests that a decline is more likely when beginning cloud-cover-anomalies are high, while an increase is more likely when beginning anomalies are low.

A direct comparison of ΔCCA between two subsets of the data would be biased by their initial distributions. Any randomly chosen group of trajectories with below-average initial-cloud-cover-anomalies would be expected to show an increase in ΔCCA, while a randomly chosen group of above average initial anomalies is likely to show a decline. Both changes would occur regardless of precipitation.

In order to directly compare the evolution of different groups of trajectories we cannot use ΔCCA. Instead we can use the consistent linear relationship in Figure 6 to predict how each trajectory would be expected to evolve in the mean solely as a function of initial-cloud-cover-anomaly. We can then subtract the predicted change from the actual change, creating a quantity of delta cloud cover independent of the initial distribution. This Difference-From-Predicted-Δ

quantity (DP-Δ) is what we use to compare groups of trajectories. We repeat this analysis for AMSR-E LWP and our MODIS-derived N_d, for which there are also consistent linear relationships between their initial values and the means of their 24-hour changes (not shown).

An example of this method would begin with a trajectory showing 80% cloud cover at hour zero (H0) and location zero (L0). The seasonal mean cloud cover at L0 is 60%, meaning the initial cloud cover anomaly (A0) is +20%. Sampling along the trajectory after 24 hours at location L24, the observed cloud cover is 50% (after adjusting for the zenith angle bias). Seasonal mean cloud cover at L24 is 45%, indicating an anomaly at 24 hours (A24) of +5%. The Δ Cloud Cover Anomaly (ΔCCA, A24-A0) is -15%. Figure 6 shows that the average of all trajectories starting with an initial anomaly of 20% would show an average decrease of 13% after 24 hours, we call this average decrease the predicted change (P-Δ). The difference from predicted (DP-Δ = ΔCCA – P-Δ) is -2%. This means that our single trajectory decreases by an additional 2% relative to the average decrease, so its difference from predicted is -2%. By grouping trajectories and comparing DP-Δ between groups we will look at whether certain environmental factors can significantly affect cloud evolution relative to the predicted change.

Our results focus on DP-Δ values only at 24 hours because the slopes for 12-hour ΔCCA vs the initial anomaly showed a significant diurnal dependence. Slopes for 12-hour changes were steeper when transitioning from day-to-night compared to night-to-day. This diurnal dependence suggests that anomalies are more persistent from night-to-day, rather than day-to-night. This night-to-day persistence was first examined in Pincus et al. (1997). Slopes for 24-hour ΔCCA did not show a significant difference from day-to-day versus night-to-night.

3. Results

Stratocumulus breakup is modulated by several variables. A comprehensive study of all variables related to cloud breakup would require a much larger sample size than we currently have available. In this work we originally set out to assess whether precipitation can act to significantly alter Sc evolution. The concurrent CloudSat and CALIPSO data show a significant positive correlation between precipitation and boundary layer depth. Further, the concurrent ECMWF-AUX data shows that PBL depth is negatively correlated with LTS, which is also shown by Wood and Hartmann (2006). To study the effects of one variable we must hold the others constant to see whether PBL depth, precipitation, LTS, or all three independently contribute to Sc breakup. Because of our limited sample size we limit our analysis to these three variables for now. We choose these three not only because they are correlated, but because each has been identified from theory and/or modeling as being potentially important for breakup, while each may act differently to alter cloud evolution (i.e. stronger stability leads to less mixing at cloud top, deeper boundary layers are decoupled leading to altered moisture and aerosol sources, and precipitation leads to altered aerosols and altered thermodynamic structure in the PBL). Beyond this study we hope to use our methods to study the effects of high clouds, upper level humidity, divergence, and other proposed causes of Sc breakup.

In Figures 7, 8, and 9 we plot DP-Δ values for two sets of trajectories, shown as the two separate lines on each panel. Sets are determined by whether the starting values of precipitation rate, LTS, or PBL depth are high or low. DP-Δ values are shown along the y-axis. Variables held constant in bins are shown along the x-axis. Bins are not uniform, but are instead chosen to have equal numbers of trajectories per bin, with 25% of the trajectories in each bin. Significant separation between the sets in the y-direction suggests that the high/low variable we use to define the sets *is* a factor in Sc breakup independent of the variable along the x-axis.

a. DP-Δ cloud cover anomalies

Figure 7a and Figure 7b show DP-Δ cloud anomalies (y-axis) for bins of constant boundary layer depth (x-axis). Trajectories are separated by above or below zero LTS-anomalies in Figure 7a while trajectories are separated by above or below median precipitation-rate (median ~0.01 mm/hr) in Figure 7b. Plots show a negative slope, indicating an inverse relationship between boundary layer depth and cloud breakup. Figure 7a shows significant separation between the high- and low-LTS trajectories. This suggests that LTS anomalies significantly affect cloud breakup independent of PBL depth, with clouds persisting under high LTS conditions. A more complex result for trajectories with above- and below-median precipitation appears in Figure 7b. The effects of precipitation on Sc breakup appear smaller than LTS, and not consistent across the bins of constant PBL depth. Precipitation may be associated with cloud persistence in shallow boundary layers while it may be associated with cloud breakup in deeper boundary layers, though the separation of the two groups is only marginally significant on either end of their overlap. The offset along the x-axis of the two sets in Figure 7b indicates that precipitation tends to be more frequent in deeper boundary layers, which is consistent with previous findings (i.e. Bretherton et al. 2010, Wood 2012). Without controlling for PBL depth, precipitation could falsely appear to be a major contributing factor in Sc breakup.

DP-Δ cloud anomalies for bins of constant LTS anomalies are shown in Figure 7c and Figure 7d. Both plots show a positive slope, supporting the results from Figure 7a that LTS is a significant factor in cloud breakup, and that positive LTS anomalies are associated with more persistent clouds. Figure 7c shows that PBL depth is a factor in cloud breakup when LTS is held

constant; cloud cover appears to be more persistent in shallow boundary layers than in deeper ones. Figure 7d shows less separation for above- and below-median precipitation, especially in high LTS, once again suggesting that precipitation is less of a factor in Sc breakup relative to PBL depth or LTS. This measure of precipitation is but one metric, however, and later we will investigate other metrics (i.e. heavy precipitation, which may be associated with cloud persistence in shallow PBLs and cloud breakup in deep PBLs).

Figure 7e and Figure 7f show DP-Δ cloud anomalies for bins of constant rain rate. Both frames show significant separation between the two groups of trajectories. This result verifies the takeaway from the prior two figures: That LTS and PBL depth are more significant factors in Sc breakup compared with precipitation, and that Sc persists in shallow boundary layers and in environments with high LTS. Three of the four plots show a slight negative slope, possibly suggesting that high rain rates may slightly favor cloud breakup, but these slopes are marginally significant at best. We investigate this in the *rain rate* section (3.e).

b. DP-Δ cloud LWP

Figure 8 follows the same template as Figure 7, but instead of DP-Δ cloud anomaly we show DP-Δ LWP. This was the lone figure that showed significantly different results when observations with interfering clouds were filtered out of the analysis, so Figure 8 is based on LWP retrievals taken only when ice clouds, unknown clouds, and multi-layered clouds were all absent from coinciding observations from the MODIS optical properties dataset. We discuss changes in LWP as changes "relative" to the evolution of all trajectories as a whole rather than as absolute changes.

The evolution of LWP behaves slightly differently than the evolution of cloud cover

anomalies in terms of sensitivity to our parameters. Separation between the two groups of trajectories in each panel in Figure 8 is generally less than those in Figure 7. Initially high LTS in shallow boundary layers (Figure 8a) or boundary layers with low rain rates (Figure 8f) is weakly associated with relatively persistent LWP. These results are not statistically significant as the standard errors show some overlap. Precipitation shows a stronger relationship with LWP than with cloud cover. Rain may lead to a relative reduction in LWP, especially in deeper boundary layers or environments with lower LTS (Figure 8b and Figure 8d). PBL depth has a similar affect on LWP as on cloud anomalies, with LWP persisting in shallow boundary layers (Figure 8c and Figure 8e).

c. DP-Δ N_d

Figure 9 once again follows the template of Figure 7 and Figure 8, but for DP-Δ of N_d anomalies. Figure 9a and Figure 9b show that N_d evolution is strongly dependent on boundary layer depth for PBLs shallower than 1.5 km. In those shallow boundary layers N_d is generally more persistent, but also dependent on LTS and perhaps precipitation, with higher stability and drier environments associated with relatively positive changes in N_d. N_d evolution in deeper boundary layers is not significantly affected by LTS or precipitation. N_d shows consistent relative declines in boundary layers deeper than 1.5 km. This is reinforced by Figure 9c and Figure 9e, both showing consistent, slightly negative DP-Δ of N_d in deep boundary layers, but positive relative changes in DP-Δ N_d in shallow boundary layers. Slopes of the shallow boundary layer plots (the black curves in Figure 9c and Figure 9d) agree with our interpretations of Figure 9a and Figure 9b, that rain and low LTS lead to relative declines in N_d, as long as the boundary layer is shallow.

d. Regional differences

We have carried out the analysis described in the prior three sub-sections for each of our regions individually. Figure 10 and Figure 11 show a subset of the figures for two of our regions from Figure 1): the Southeast Pacific and the Eastern Indian Ocean. The figures are arranged identically. These subsets are shown because they exhibit somewhat different behavior relative to the all-region aggregates shown in Figure 7-Figure 9.

The southeast Pacific is shown if Figure 10. Figure 10a and Figure 10b show DP-Δ of cloud cover anomalies for groups of high and low LTS and high and low rain rate for bins of constant PBL depth. Figure 10a shows agreement with our prior results: Low LTS is associated with cloud breakup. The rain rate breakdown (Figure 10b) shows a distinctly different relationship for this region: Clouds persist with increased precipitation, especially in shallower boundary layers. Figure 10c and Figure 10d show PBL depth and high and low rain rate for bins of constant LTS anomaly. The almost perfect overlap in Figure 10c suggests that PBL depth is not a significant factor in cloud breakup over the Southeast Pacific. Figure 10d again shows that higher rain rates over the Southeast Pacific lead to cloud persistence.

Figure 11 shows that Sc breakup over the Eastern Indian Ocean is likely driven by different forcings than the Southeast Pacific. Figure 11a and Figure 11c show that LTS anomalies may not affect Sc breakup, while PBL depth does affect breakup. Figure 11b and Figure 11d show that higher rain rates are associated with Sc breakup.

We do not show the regional breakdowns for LWP and N_d. Liquid water path does not show consistent results when broken down by region. LWP shows the widest error bars and least separation between sets (Figure 8) and this is exacerbated with smaller sample sizes for a

regional breakdown. Results for N_d evolution for each region are much more consistent, with all of the aforementioned relationships remaining intact even when broken down by region.

e. Rain Rate

Precipitation may have a subtle contribution to cloud breakup or persistence depending on boundary layer depth, as hinted at in Figure 7b. There are different aspects of precipitation that might influence PBLs in different ways (i.e. Wang and Feingold 2009, and Wood 2012 find that it is heavy precipitation reaching the surface that causes a closed to open cell transition). Clouds in shallow boundary layers appear to be more persistent with than without precipitation while clouds in deep boundary layers break up faster with precipitation. We investigate this further in Figure 12, which includes rain rate in the analysisså. Figure 12 shows three curves, one for below-median rain-rate (rate < 0.01mm/hr, green), above-median moderate rain (0.01 < rate < 0.055 mm/hr, blue), and one for "heavy" rain (rate > 0.055 mm/hr, black).

The plots in Figure 12 support our earlier result that rain leads to cloud persistence in shallow PBLs, but possibly to breakup in deeper PBLs. Trajectories starting with below-median rain rates (green) show a lower slope than for trajectories starting with above-median rain rates (blue & black). Increasing the rain rate appears to lead to a steeper negative slope, which means that heavier rain in a shallow boundary layer leads to more Sc persistence while heavier rain in a deeper boundary layer leads to greater Sc decline. For shallow boundary layers, this relationship could be due to the heavy precipitation falling in areas of open cellular convection where a further decrease in cloud cover is not likely.

We examined a simpler version of Figure 12 for each region, with trajectories grouped by above or below median rain rate. All plots showed the same pattern of negative slopes as seen in

Figure 12, again with the high rain rate group showing a more negative slope in each region. Once again, this suggests that a higher rain rate may exacerbate the subtle effects of precipitation, leading to more Sc persistence in shallow PBLs, but to Sc breakup in deeper PBLs.

4. Discussion and Conclusions

In this work we tackle several problems with the data and methods that could lead to biases in our analysis. A seasonal and geographic bias is reduced by using seasonal anomalies for all three of the variables we tracked. Satellite zenith angle biases are identified and removed. Most importantly, we have created a variable (DP-Δ) that allows us to directly compare the evolution of Sc in groups of trajectories with differing initial cloud properties. The linear relationship between starting CCA and ΔCCA may be useful in future work to examine decorrelation time and Lagrangian timescales in Sc decks.

The evolution of marine Sc is modulated by several factors. Changes in cloud amount (and therefor albedo) appear to be affected more by the boundary layer depth and the lower tropospheric stability and less by precipitation. Sc in deeper boundary layers or in less stable environments appears to break up more readily than in shallow boundary layers or stable environments. This was seen when when PBL depth or LTS was held constant, indicating that these factors work somewhat independently of one-another. The result that deeper PBLs tend to break up more quickly, although expected from our basic theory of decoupling and breakup (Bretherton and Wyant 1997), has not to our knowledge been previously reported in a Lagrangian study. The result that lower LTS leads to Sc breakup agrees with Sandu et al. 2010.

We propose a few physical processes associated with our results: That strong inversions may inhibit dry-air entrainment at cloud top causing Sc to persist. Moisture and aerosol

transport into the Sc layer may be limited in deep, decoupled boundary layers, while strong Cu updrafts into decoupled Sc decks may enhance entrainment and disrupt the thermodynamically driven circulation leading to cloud breakup. There are regional preferences as to which factor controls Sc breakup. PBL depth is a significant driver of Sc breakup in the East Indian Ocean while LTS is not, but the opposite is true in the Southeast Pacific. Both factors are significant in the NE Pacific and SE Atlantic. Burleyson and Yuter (2015, in press) saw a similar grouping of regions when looking at differences in diurnal cycles, with the SE Pacific behaving differently relative to the NE Pacific and SE Atlantic.

The evolution of area-averaged liquid water path appears to be more sensitive to PBL depth and precipitation, but less sensitive to the initial LTS anomaly. In shallow boundary layers LWP and cloud amount show an opposing reaction to increased precipitation, with clouds persisting, but thinning. We speculate that the precipitation may thin the clouds and lower the LWP, but that the overturning associated with drizzle formation allows the clouds to persist.

The effect of precipitation on the evolution of Sc still appears complex. Further modeling studies focusing on precipitation intensity are needed. Figure 7b and Figure 12 show that rain may lead to cloud persistence in shallow boundary layers or cloud break-up in deeper boundary layers, though significance appears marginal. Heavier rain appears to enhance this effect. Regionally, precipitation showed little consistency when PBL depth was accounted for: Rain showed little significant effect in the Northeast Pacific, and Southeast Atlantic. Rain is associated with cloud persistence in the Southeast Pacific, but with cloud breakup in the East Indian Ocean. It is noteworthy that average PBL depth is 300 meters deeper in the East Indian Ocean relative to the Southeast Pacific. Future work will focus on determining what environmental factors modulate the effects of rain on Sc evolution and why and how the

relationships vary regionally.

Precipitation does affect LWP and N_d, leading to a relative decline in both. The explanation may be as simple as the physical removal of liquid water and aerosol (Albrecht 1989, Wood et al. 2012) from the cloud layer. The decline in N_d related to precipitation is only seen when the PBL is shallow; N_d appears to be affected by very little in deeper boundary layers where it shows a consistent relative decline. This may be the case because the cloud layer in a deeper decoupled PBL is partially cut off from the aerosol source at the sea surface. Future work may focus on estimating entrainment for each trajectory.

Results from this work support many existing hypotheses about Sc evolution (i.e. decoupled boundary layers tend to break up, weaker inversions are associated with Sc breakup, and precipitation rate plays an important, but complex role in breakup) while inviting further research with a larger sample size. Many of the proposed mechanisms appear to have a significant affect on Sc evolution. We hope to further this work using more A-Train products and meteorological data to study more proposed mechanisms for Sc break up and to attempt to quantify the radiative and climatological effects.

Acknowledgements

This work was supported by NASA grant NNXBAQ35G (CloudSat and CALIPSO science team). Productive collaboration and discussion was provided by Sandra Yuter, Casey Burleyson, Christopher Bretherton, Christopher Terai, Johannes Mohrmann, and Irina Sandu. Rhea George provided valuable trajectory software.

References

Albrecht, B., 1989: Aerosols, cloud microphysics, and fractional cloudiness. *Science*, **245**, 1227-1230.

Bennartz, R., 2007: Global assessment of marine boundary layer cloud droplet number concentration from satellites. *J. Geophys. Res*., **112**, D02201, doi:10.1029/2006JD007547.

Boers, R., Acarreta, J. A., and Gras, J. L., 2006: Satellite monitoring of the first indirect aerosol effect: Retrieval of the droplet concentration of water clouds. *J. Geophys. Res*., **111**, D22208, doi:10.1029/2005JD006838.

Bretherton, C. S., and M. Wyant, 1997: Moisture transport, lower tropospheric stability, and decoupling of cloud-topped boundary layers. *J. Atmos. Sci.,* **54**, 148-167.

Bretherton, C. S., R. Wood, R. C. George, D. Leon, G. Allen, and X. Zheng, 2010: Southeast Pacific stratocumulus clouds, precipitation and boundary layer structure sampled along 20° S during VOCALS-Rex, *Atmos. Chem. Phys*., **10**, 10639–10654.

Burleyson, C. D. and S. E. Yuter, 2015: Sub-diurnal stratocumulus cloud fraction variability and sensitivity to precipitation. *J. Climate*, conditionally accepted, in press.

Comstock, K. K., C. S. Bretherton, and S. E. Yuter, 2005: Mesoscale variability and drizzle in southeast Pacific stratocumulus. *J. Atmos. Sci.*, **62**, 3792-3807.

Dee, D. P., and 35 co-authors, 2011: The ERA-Interim reanalysis: Configuration and performance of the data assimilation system. *Quart. J. R. Meteorol. Soc.*, **137**, 553-597.

Hahn, C. J., and S. G. Warren, 2007: A Gridded Climatology of Clouds over Land (1971-96) and Ocean (1954-97) from Surface Observations Worldwide. Numeric Data Package NDP-026E, CDIAC, Department of Energy, Oak Ridge, Tennessee.

Hartmann, D. L., and D. A. Short, 1980: On the use of Earth Radiation Budget statistics for studies of clouds and climate. *J. Atmos. Sci*., **17**, 1233-1250.

Hubanks, P. A., M. D. King, S. Platnick, and R. Pincus, 2008: MODIS Atmosphere L3 Gridded Product Algorithm Theoretical Basis Document. *ATBD Reference Number: ATBD-MOD-30.*

Klein, S. A., D. L. Hartmann, and J. R. Norris, 1995: On the relationship among low-cloud structure, sea surface temperature, and atmospheric circulation in the summertime Northeast Pacific. *J. Climate*, **8**, 1140-1155.

Lebsock, M. D., and T. S. L'Ecuyer, 2011: The retrieval of warm rain from CloudSat*, J. Geophys. Res*., **116**, D20209, doi:10.1029/2011JD016076.

Maddux, B. C., S. A. Ackerman, and S. Platnick, 2010: Viewing geometry dependencies in

MODIS cloud products. *J. Atmos. Ocean Technol.*, **27**, 1519-1528.

Martin, G. M., D. W. Johnson, and A. Spice, 1994: The measurement and parameterization of effective radius of droplets in warm stratocumulus clouds. *J. Atmos. Sci*., **51**, 1823-1842.

Mechem, D. B., and Y. L. Kogan, 2003: Simulating the transition from drizzling marine stratocumulus to boundary layer cumulus with a mesoscale model. *Mon. Wea. Rev*. **131**, 2342-2360.

Mitrescu, C., T. L'Ecuyer, J. Haynes, S. Miller, and J. Turk, 2010: Cloud-Sat precipitation profiling algorithm: Model description. J. Appl. *Meteorol. Climatol.*, **49**, 991-1003.

Myers, T. A. and J. R. Norris, 2013: Observational evidence that enhanced subsidence reduces subtropical marine boundary layer cloudiness. *J. Climate*, **26**, 7505-7524.

Oreopoulous, L., 2005: The impact of subsampling on MODIS level-3 statistics of cloud optical thickness and effective radius. *IEEE Transactions on Geoscience and Remote Sensing*, **43(2)**, 366-373.

Pincus, R., M. B. Baker, and C. S. Bretherton, 1997: What controls stratocumulus radiative properties? Lagrangian observations of cloud evolution. *J. Atmos. Sci*., **54**, 2215-2236.

Sandu, I., B. Stevens, and R. Pincus, 2010: On the transitions in marine boundary layer

cloudiness. *Atmos. Chem. Phys*., **10**, 2377-2391.

Sandu, I. and B. Stevens, 2011: On the factors modulating the stratocumulus to cumulus transitions. *J. Atmos. Sci.,* **68**, 1865-1881.

Stevens, B., W. R. Cotton, G. Feingold, and C-H Moeng, 1998: Large-eddy simulations of strongly precipitating, shallow, stratocumulus-topped boundary layers. *J. Atmos. Sci.,* **55**, 3616-3638.

Stevens, B., G. Vali, K. Comstock, R. Wood, M. VanZanten, P. H. Austin, C. S. Bretherton, and D. H. Lenschow, 2005: Pockets of open cells (POCs) and drizzle in marine stratocumulus. *Bull. Amer. Meteor. Soc.*, **86**, 51-57.

Vaughan, M., S. Young, D. Winker, K. Powell, A. Omar, Z. Liu, Y. Hu, and C. Hostetler, 2004: Fully automated analysis of space-based lidar data: an overview of the CALIPSO retrieval algorithms and data products. *SPIE Int. Soc. Opt. Eng.*, **5575**, 16-30.

Wang, H. and G. Feingold, 2009: Modeling Mesoscale Cellular Structures and Drizzle in Marine Stratocumulus. Part I: Impact of Drizzle on the Formation and Evolution of Open Cells. *J. Atmos. Sci.*, **66**, 3237–3256.

Wentz, F. J. and T. Meissner. 2004: AMSR-E/Aqua L2B Global Swath Ocean Products derived from Wentz Algorithm. Version 2. [L3 LWP]. Boulder, Colorado USA.

Wood, R., 2000: Parametrization of the effect of drizzle upon the droplet effective radius in stratocumulus clouds. *Q. J. R. Meteorol. Soc*., **126**, 3309-3324.

Wood, R., and C. S. Bretherton, 2004: Boundary layer depth, entrainment, and decoupling in the cloud-capped subtropical and tropical marine boundary layer. *J. Climate*, **17**, 3576-3588.

Wood, R., and D. L. Hartmann, 2006: Spatial variability of liquid water path in marine low cloud: the importance of mesoscale cellular convection. *J. Climate*, **19**, 1748-1764.

Wood, R., 2012: Stratocumulus clouds. *Mon. Wea. Rev*., **140**, 2373-2423.

Wood, R., D. Leon, M. Lebsock, J. Snider, and A. D. Clarke, 2012: Precipitation driving droplet concentration variability in low clouds. *J. Geophys. Res*., **117**, D19210.

Xiao, H., C. M. Wu, and C. R. Mechoso, 2011: Buoyancy reversal, decoupling, and the transition from stratocumulus to shallow cumulus topped marine boundary layers. *Clim. Dyn*., **37**, 971-984.

Zhou, X., P. Kollias, and E. Lewis, 2015: Clouds, precipitation and marine boundary layer structure during the MAGIC field campaign. *J. Climate*. doi:10.1175/JCLI-D-14-00320.1, in press.

Figure Captions

Figure 1. A smoothed contour plot showing the yearly average, daytime mean Sc amount between 45° North and South. Ocean data is the average for the period 1954-1997, land data is for the period 1971-1996. Cloud amount is reported by surface observers either on ships or at weather stations. The red boxes show our regions of study. We only use the ocean portions of the boxes.

Figure 2. An example 30-hour trajectory from the Northeast Pacific beginning January 6, 2007 at 10:59 UTC. The trajectory is shown in black. The gray arrows represent the mean wind field at 925 hPa. The dashed black line in the top figure shows the CloudSat/CALIPSO track. The 100km sampling radius is shown to scale by the circles in each frame. The Aqua satellite track (carrying both MODIS and AMSR/E instruments) is shown by the solid colored lines. The MODIS swath is shown by the colored regions surrounding the Aqua track. Only MODIS data from Aqua is used.

Figure 3. (a & b): Plots of CALIPSO VFM "cloud" returns within the marine boundary layer for two separate samples. The red lines indicate the cloud top height assigned using our routine. Lines in (b) are dashed, indicating multiple relevant peaks in the frequency distribution. Our routine assigns the boundary layer depth to the highest relevant peak (c): The frequency distribution for cloud top heights shown in b.

Figure 4. The mean cloud amount and standard error for each 10° zenith angle over the regions shown in Figure 1. Polynomial fits to the mean cloud amounts are shown as black, red, and blue

curves. The red and blue X's show how precipitating trajectories (blue) are observed at lower zenith angles after 24 hours compared to non-precipitating trajectories (red).

Figure 5. The relative frequency of precipitating and non-precipitating samples for bins of starting cloud cover anomalies. Precipitating samples are defined as having any precipitation observed at the surface over their entire 200km extent.

Figure 6. Δ Cloud cover anomaly for bins of initial cloud cover anomalies for all trajectories at 12- and 24-hours. Slopes are calculated using robust multilinear regression.

Figure 7. DP-Δ cloud cover anomalies for bins of constant boundary layer depth (a-b), LTS anomalies (LTS', c-d), and rain rate (e-f). Trajectories are broken into two sets for each plot, with high (>0) and low (<0) LTS anomalies (a,f); above and below median (~ 0.01mm/hr) rain rates; and shallow (<1.5km) versus deep (>1.5km) boundary layers. Thick lines are the mean DP-Δ cloud cover anomalies, thin lines show the standard error (1-σ) of the mean. Bins are not uniform, but are instead chosen to have equal numbers of trajectories per bin, with 25% of the trajectories in each bin.

Figure 8. DP-Δ liquid water path anomalies for bins of constant boundary layer depth (a-b), LTS anomalies (LTS', c-d), and rain rate (e-f). Trajectories are broken into two sets for each plot, with high (>0) and low (<0) LTS anomalies (a,f); above and below median (~ 0.01mm/hr) rain rates; and shallow (<1.5km) versus deep (>1.5km) boundary layers. Thick lines are the mean DP-Δ LWP, thin lines show the standard error (1-σ) of the mean. Bins are not uniform, but are instead chosen to have equal numbers of trajectories per bin, with 25% of the trajectories in each

bin. LWP observations are only used if concurrent amounts of high, unknown, and multi-layered clouds are all equal to zero.

Figure 9. DP-Δ N_d anomalies for bins of constant boundary layer depth (a-b), LTS anomalies (c-d), and rain rate (e-f). Trajectories are broken into two sets for each plot, with high (>0) and low (<0) LTS anomalies (a,f); above and below median (~ 0.01mm/hr) rain rates (b,d); and shallow (<1.5km) versus deep (>1.5km) boundary layers (c,e). Thick lines are the mean DP-Δ N_d, thin lines show the standard error (1-σ) of the mean. Bins are not uniform, but are instead chosen to have equal numbers of trajectories per bin, with 25% of the trajectories in each bin.

Figure 10. DP-Δ cloud cover anomalies for bins of constant PBL depth (a-b), and LTS anomalies (LTS', c-d) over the Southeast Pacific. Trajectories are broken into two categories for each panel: High (>0) and low (<0) LTS anomalies (a), above and below median rain rate (b, d), and deep (>1.5km) and shallow (<1.5km) PBL depth (c). Thick lines are the mean DP-Δ cloud cover anomalies, thin lines show the standard error (1-σ) of the mean. Bins are not uniform, but are instead chosen to have equal numbers of trajectories per bin, with 33% of the trajectories in each bin.

Figure 11. DP-Δ cloud cover anomalies for bins of constant PBL depth (a-b), and LTS anomalies (LTS', c-d) over the Eastern Indian Ocean. Trajectories are broken into two categories for each panel: High (>0) and low (<0) LTS anomalies (a), above and below median rain rate (b, d), and deep (>1.5km) and shallow (<1.5km) PBL depth (c). Thick lines are the mean DP-Δ cloud cover anomalies, thin lines show the standard error (1-σ) of the mean. Bins

are not uniform, but are instead chosen to have equal numbers of trajectories per bin, with 33% of the trajectories in each bin.

Figure 12. DP-Δ cloud cover anomalies for bins of constant cloud top height/PBL depth. Trajectories are divided into three groups based on the sample-mean rain rate at the beginning of the trajectory: Below median rain rate (green), 'moderate' rain rate (blue), and 'heavy' rain rate (black). Thick lines are the mean DP-Δ cloud cover anomalies, thin lines show the standard error (1-σ) of the mean. Bins are not uniform, but are instead chosen to have equal numbers of trajectories per bin, with 33% of the trajectories in each bin.

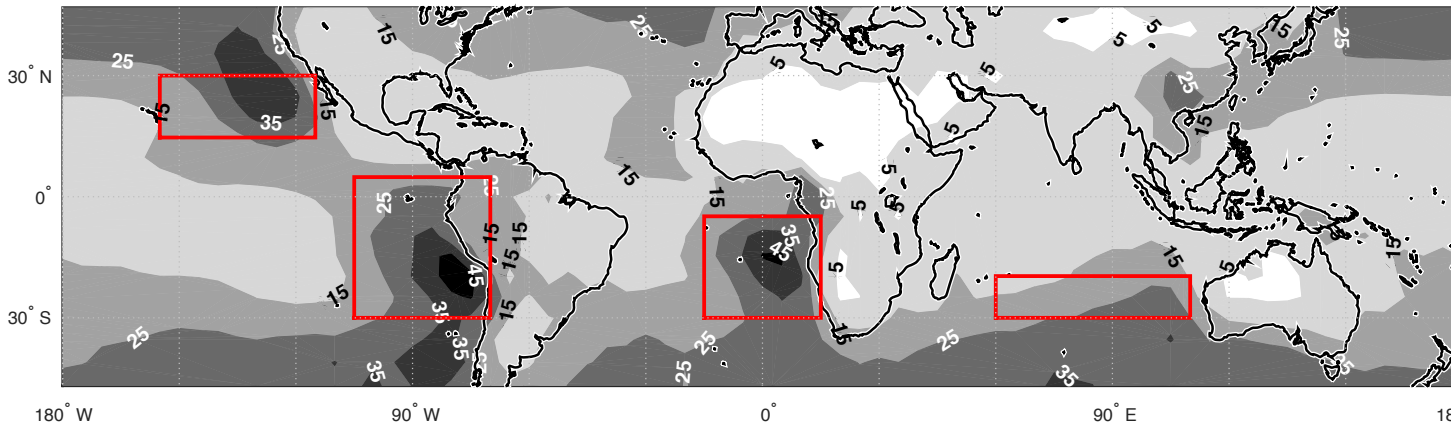

Figure 1. A smoothed contour plot showing the yearly average, daytime mean Sc amount between 45° North and South. Ocean data is the average for the period 1954-1997, land data is for the period 1971-1996. Cloud amount is reported by surface observers either on ships or at weather stations. The red boxes show our regions of study. We only use the ocean portions of the boxes.

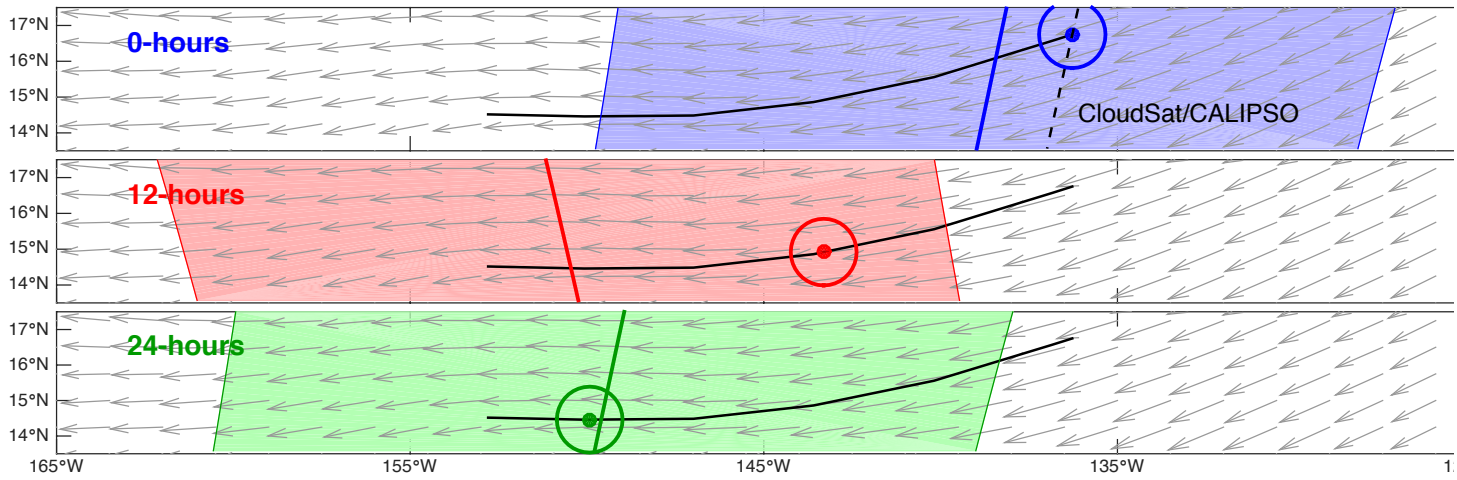

Figure 2. An example 30-hour trajectory from the Northeast Pacific beginning January 6, 2007 at 10:59 UTC. The trajectory is shown in black. The gray arrows represent the mean wind field at 925 hPa. The dashed black line in the top figure shows the CloudSat/CALIPSO track. The 100km sampling radius is shown to scale by the circles in each frame. The Aqua satellite track (carrying both MODIS and AMSR/E instruments) is shown by the solid colored lines. The MODIS swath is shown by the colored regions surrounding the Aqua track. Only MODIS data from Aqua is used.

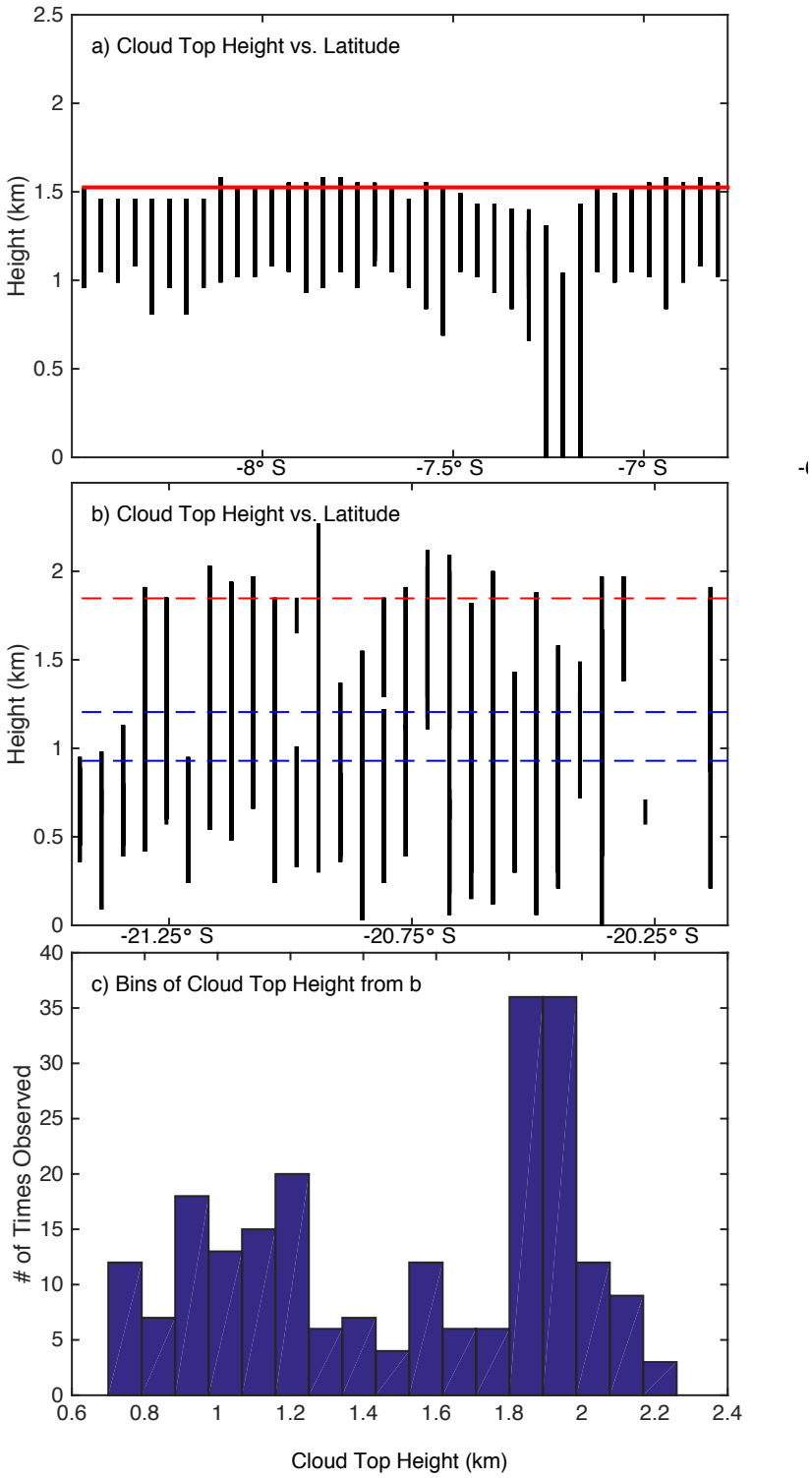

Figure 3. (a & b): Plots of CALIPSO VFM "cloud" returns within the marine boundary layer for two separate samples. The red lines indicate the cloud top height assigned using our routine. Lines in (b) are dashed, indicating multiple relevant peaks in the frequency distribution. Our routine assigns the boundary layer depth to the highest relevant peak (c): The frequency distribution for cloud top heights shown in b.

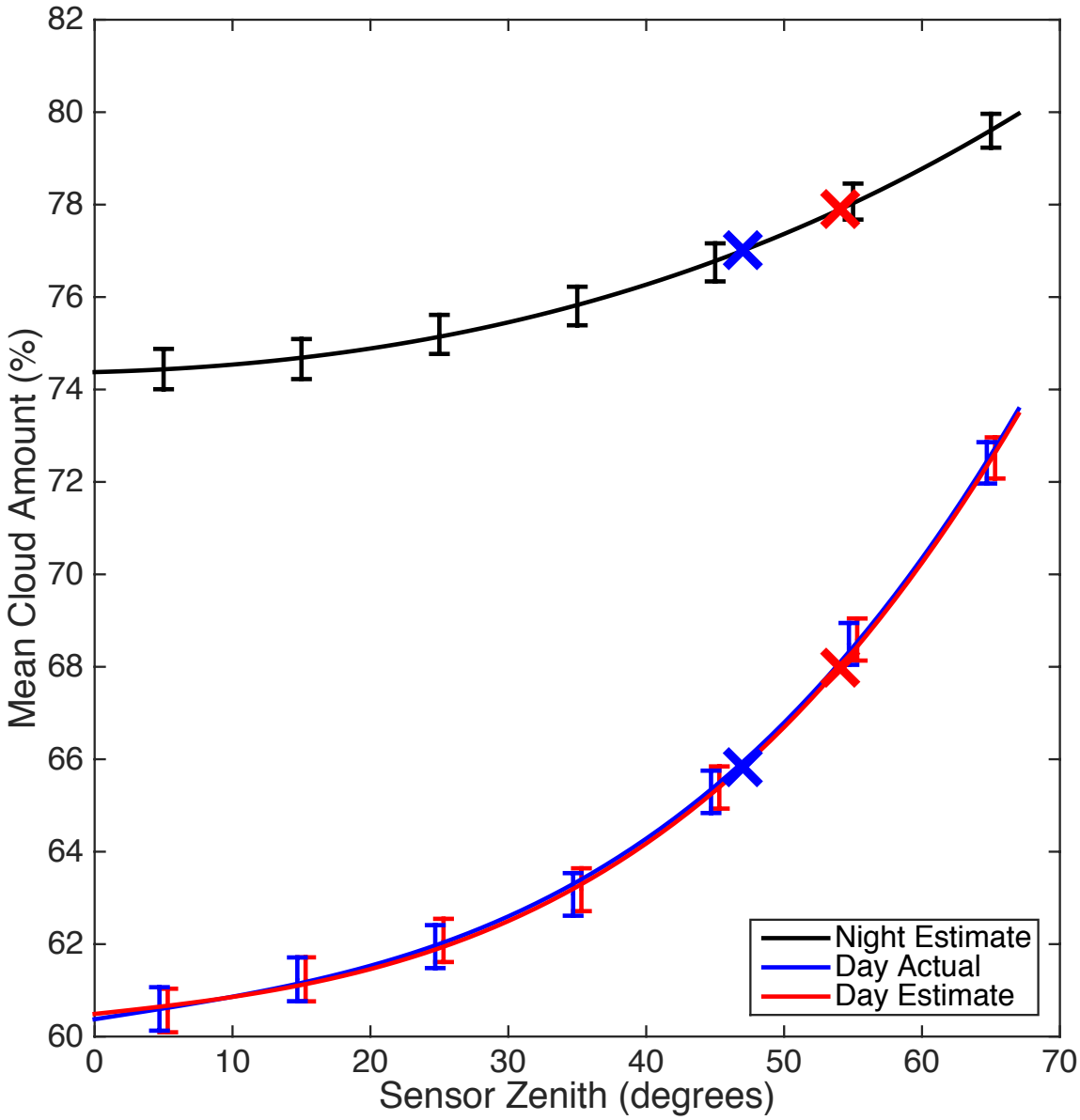

Figure 4. The mean cloud amount and standard error for each 10° zenith angle over the regions shown in Figure 1. Polynomial fits to the mean cloud amounts are shown as black, red, and blue curves. The red and blue X's show how precipitating trajectories (blue) are observed at lower zenith angles after 24 hours compared to non-precipitating trajectories (red).

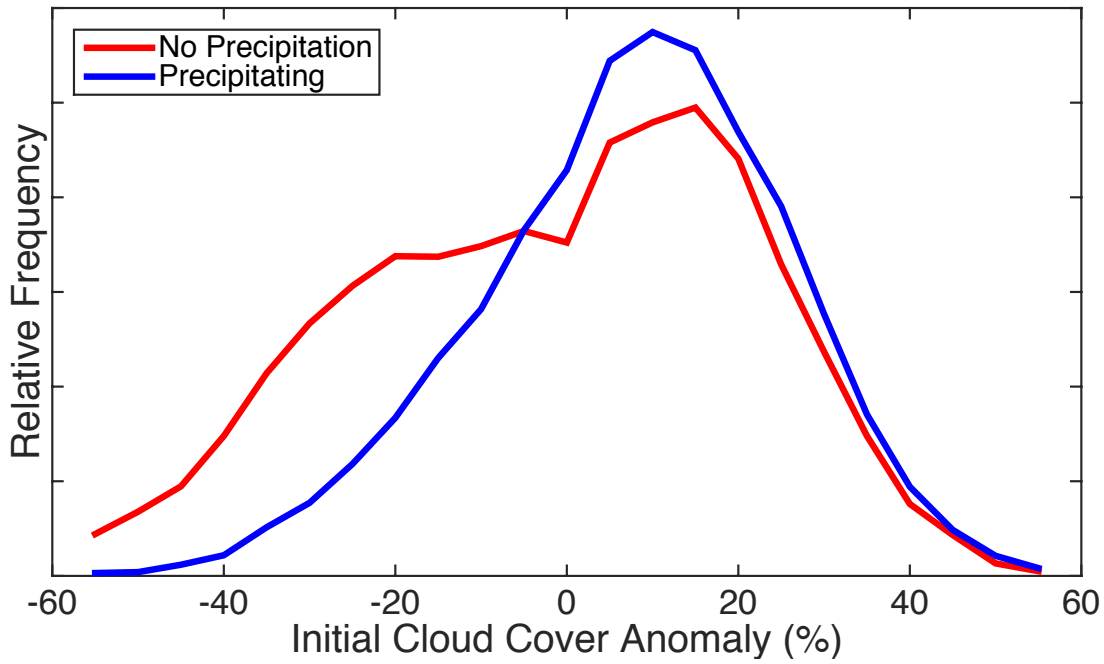

Figure 5. The relative frequency of precipitating and non-precipitating samples for bins of starting cloud cover anomalies. Precipitating samples are defined as having any precipitation observed at the surface over their entire 200km extent.

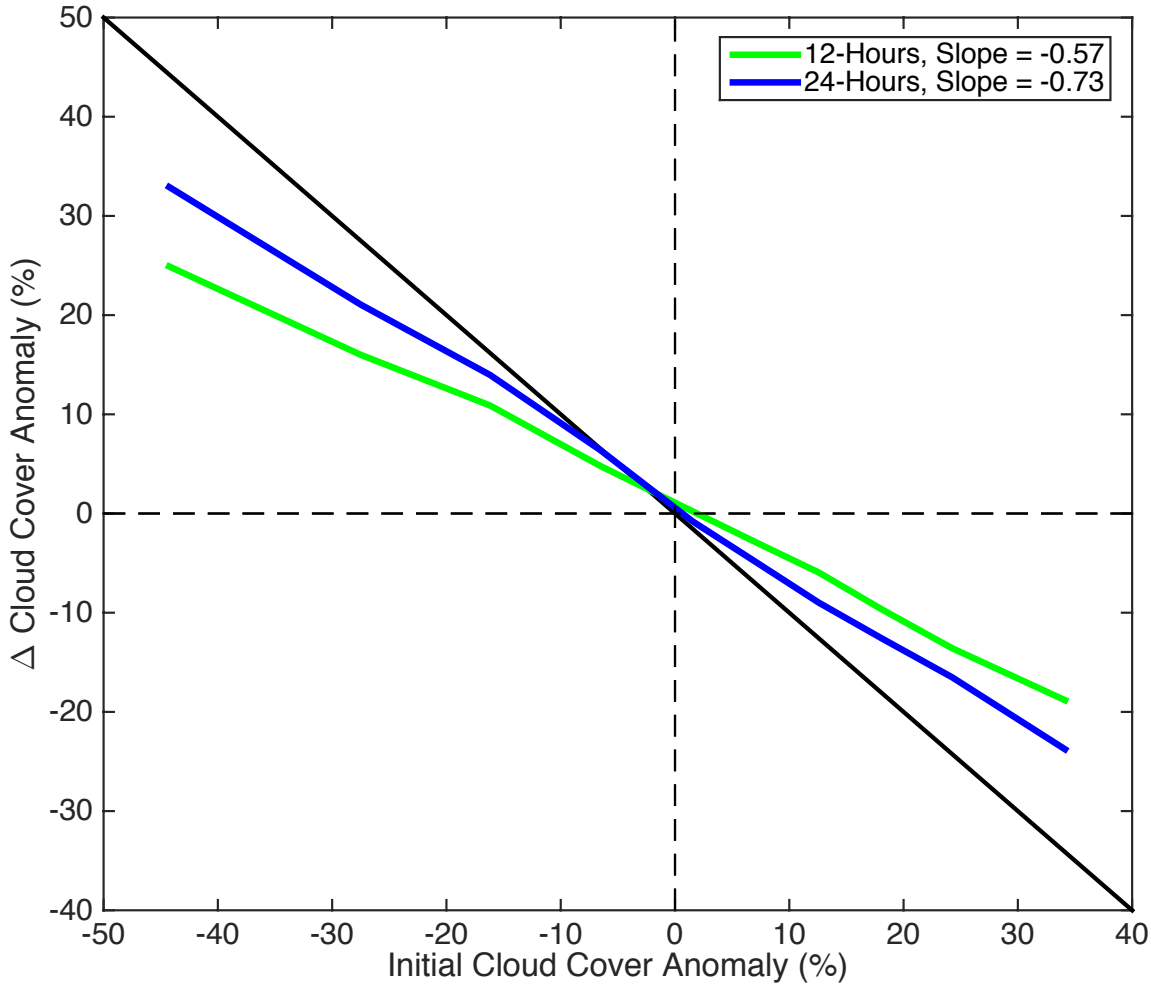

Figure 6. Δ Cloud cover anomaly for bins of initial cloud cover anomalies for all trajectories at 12- and 24-hours. Slopes are calculated using robust multilinear regression.

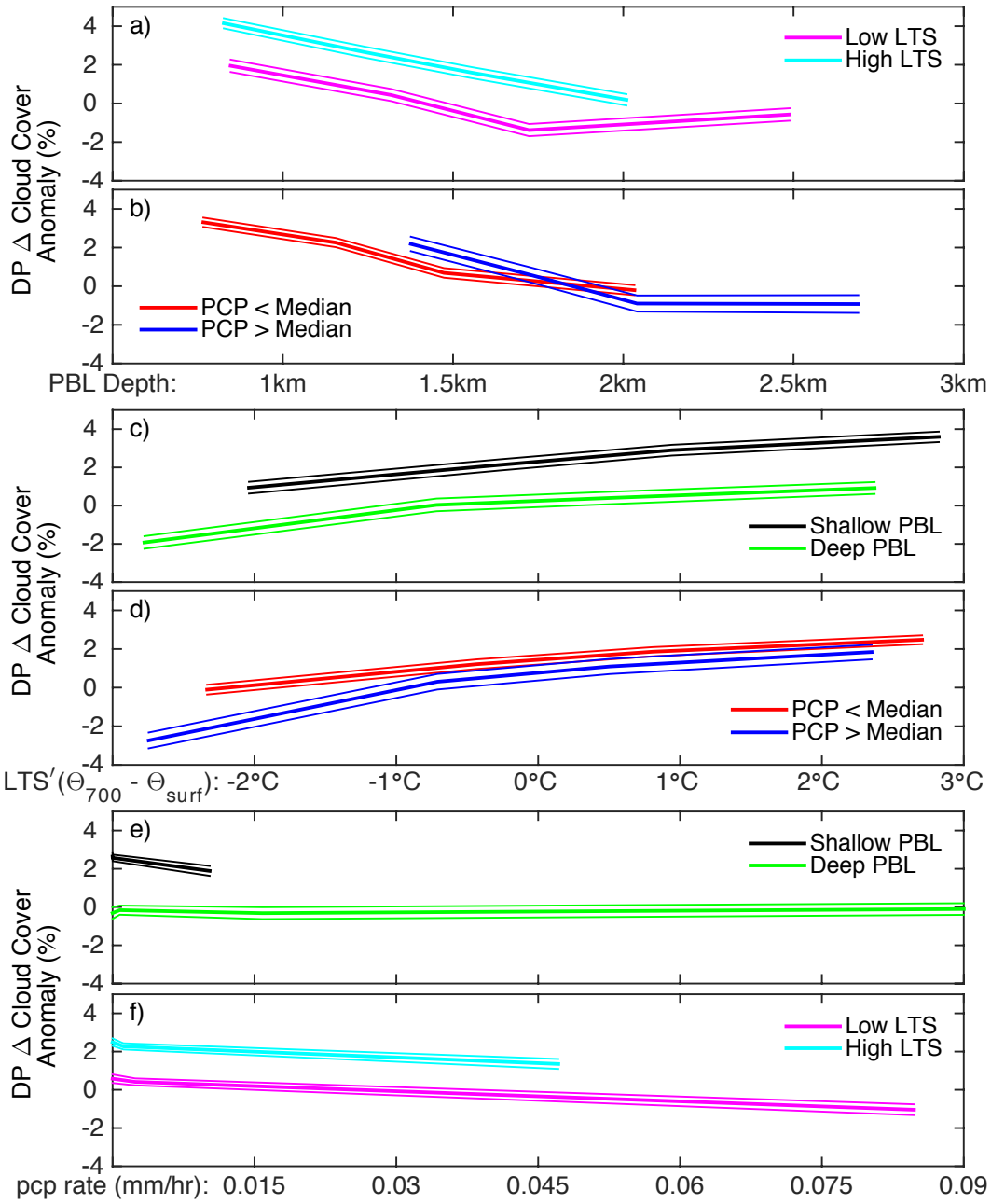

Figure 7. DP-Δ cloud cover anomalies for bins of constant boundary layer depth (a-b), LTS anomalies (LTS', c-d), and rain rate (e-f). Trajectories are broken into two sets for each plot, with high (>0) and low (<0) LTS anomalies (a,f); above and below median (~ 0.01mm/hr) rain rates; and shallow (<1.5km) versus deep (>1.5km) boundary layers. Thick lines are the mean DP-Δ cloud cover anomalies, thin lines show the standard error (1-σ) of the mean. Bins are not uniform, but are instead chosen to have equal numbers of trajectories per bin, with 25% of the trajectories in each bin.

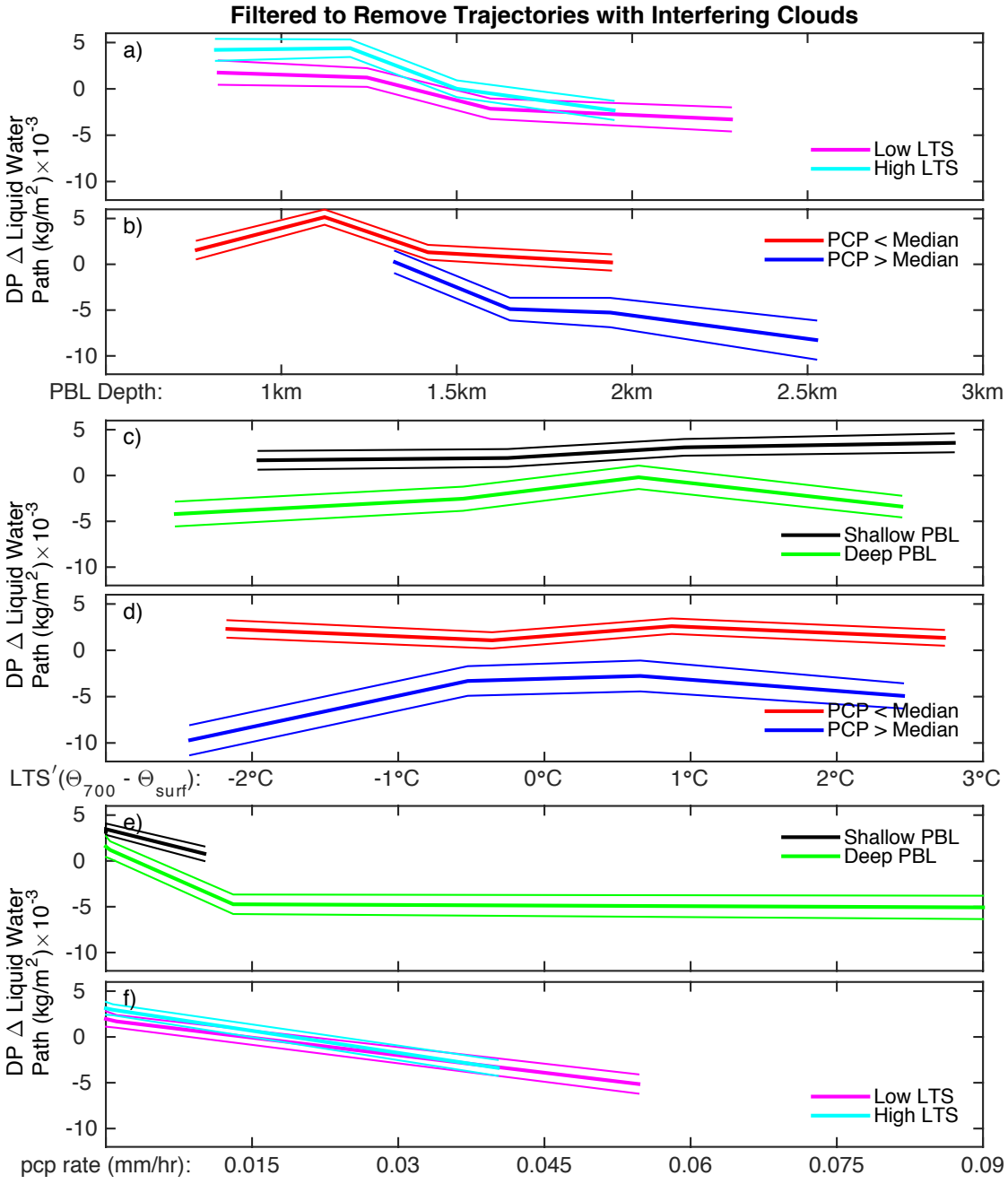

Figure 8. DP-Δ liquid water path anomalies for bins of constant boundary layer depth (a-b), LTS anomalies (LTS', c-d), and rain rate (e-f). Trajectories are broken into two sets for each plot, with high (>0) and low (<0) LTS anomalies (a,f); above and below median (~ 0.01mm/hr) rain rates; and shallow (<1.5km) versus deep (>1.5km) boundary layers. Thick lines are the mean DP-Δ LWP, thin lines show the standard error (1-σ) of the mean. Bins are not uniform, but are instead chosen to have equal numbers of trajectories per bin, with 25% of the trajectories in each bin. LWP observations are only used if concurrent amounts of high, unknown, and multi-layered clouds are all equal to zero.

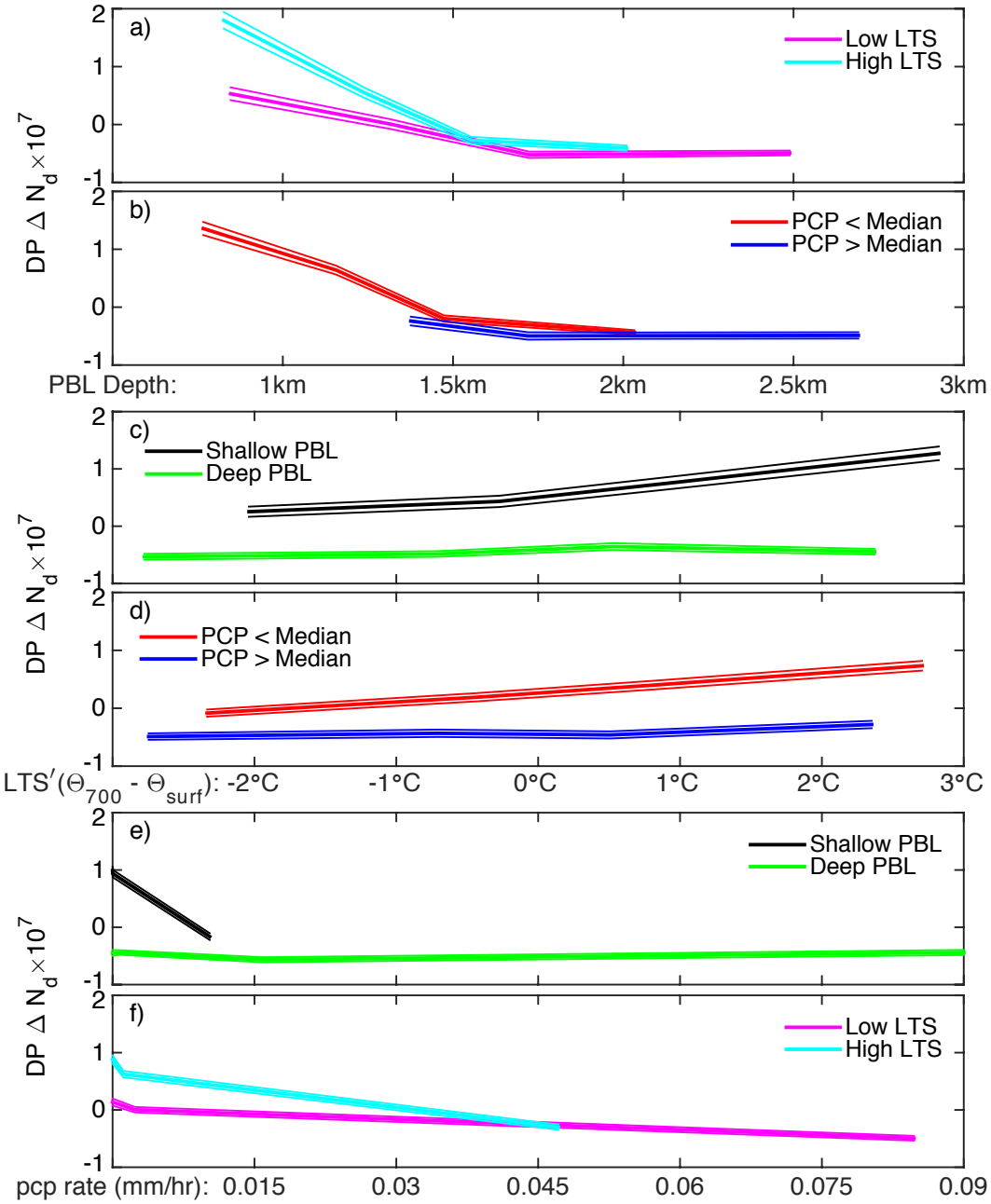

Figure 9. DP-Δ N_d anomalies for bins of constant boundary layer depth (a-b), LTS anomalies (c-d), and rain rate (e-f). Trajectories are broken into two sets for each plot, with high (>0) and low (<0) LTS anomalies (a,f); above and below median (~ 0.01mm/hr) rain rates (b,d); and shallow (<1.5km) versus deep (>1.5km) boundary layers (c,e). Thick lines are the mean DP-Δ N_d, thin lines show the standard error (1-σ) of the mean. Bins are not uniform, but are instead chosen to have equal numbers of trajectories per bin, with 25% of the trajectories in each bin.

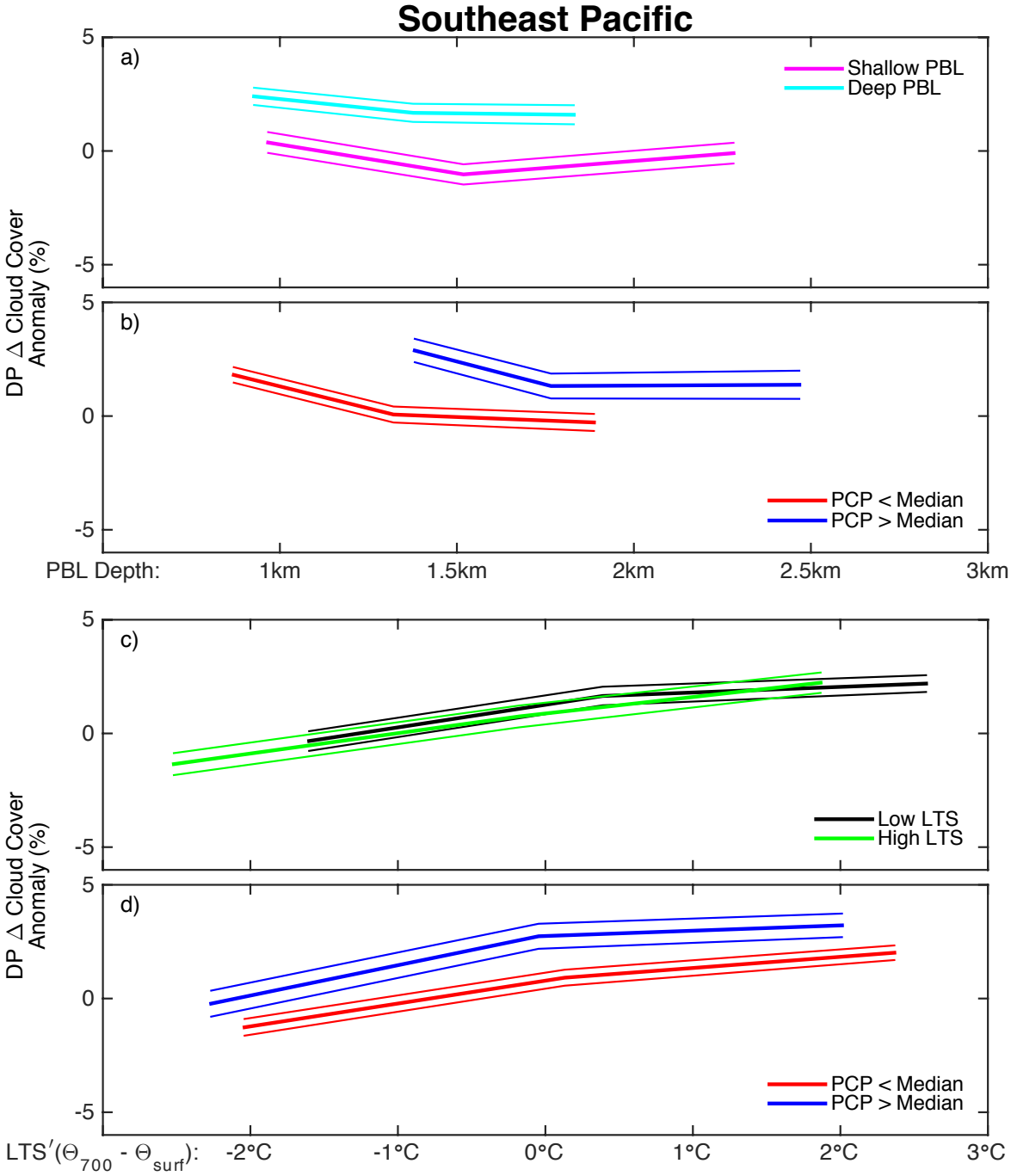

Figure 10. DP-Δ cloud cover anomalies for bins of constant PBL depth (a-b), and LTS anomalies (LTS', c-d) over the Southeast Pacific. Trajectories are broken into two categories for each panel: High (>0) and low (<0) LTS anomalies (a), above and below median rain rate (b, d), and deep (>1.5km) and shallow (<1.5km) PBL depth (c). Thick lines are the mean DP-Δ cloud cover anomalies, thin lines show the standard error (1-σ) of the mean. Bins are not uniform, but are instead chosen to have equal numbers of trajectories per bin, with 33% of the trajectories in each bin.

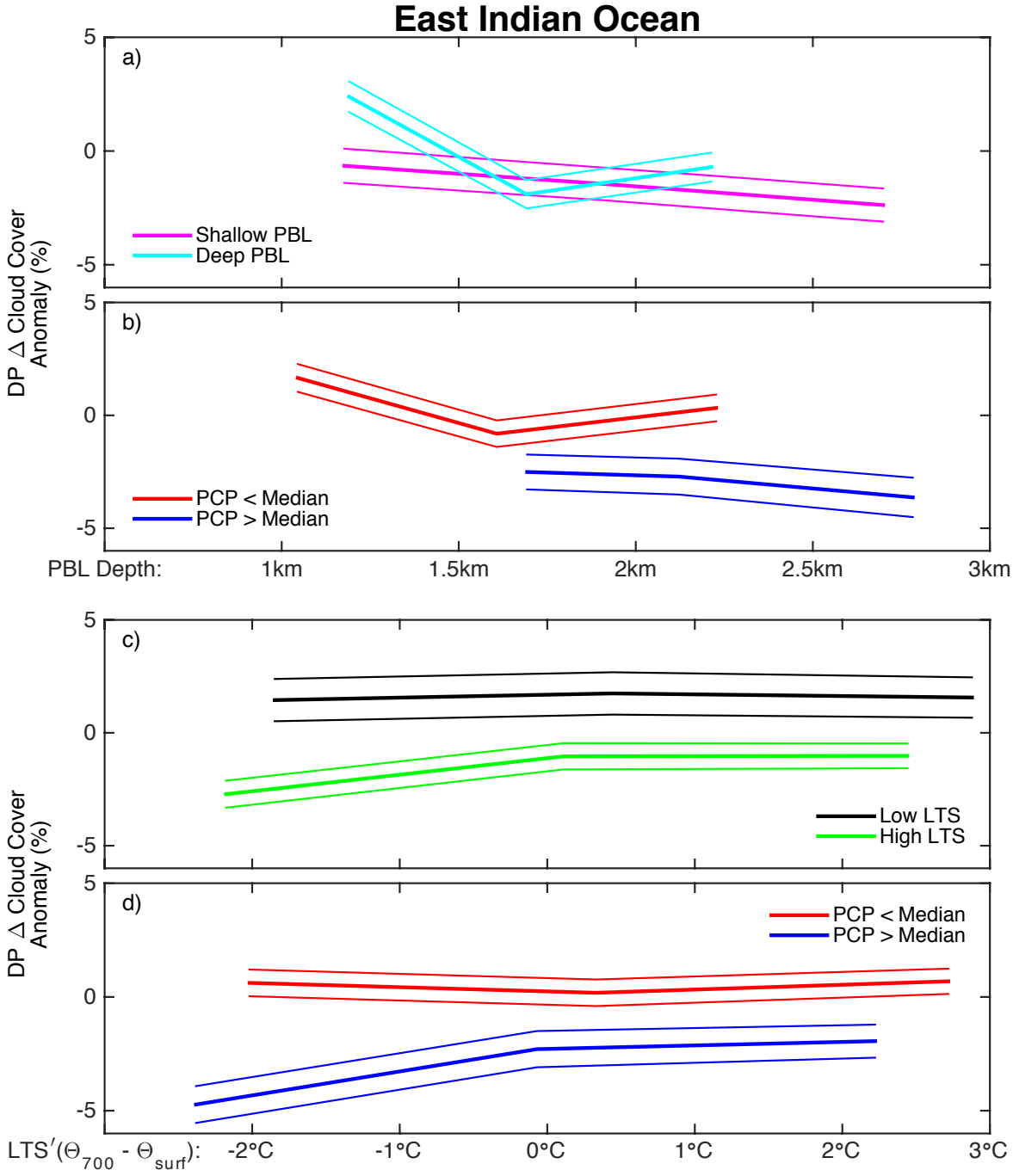

Figure 11. DP-Δ cloud cover anomalies for bins of constant PBL depth (a-b), and LTS anomalies (LTS', c-d) over the Eastern Indian Ocean. Trajectories are broken into two categories for each panel: High (>0) and low (<0) LTS anomalies (a), above and below median rain rate (b, d), and deep (>1.5km) and shallow (<1.5km) PBL depth (c). Thick lines are the mean DP-Δ cloud cover anomalies, thin lines show the standard error (1-σ) of the mean. Bins are not uniform, but are instead chosen to have equal numbers of trajectories per bin, with 33% of the trajectories in each bin.

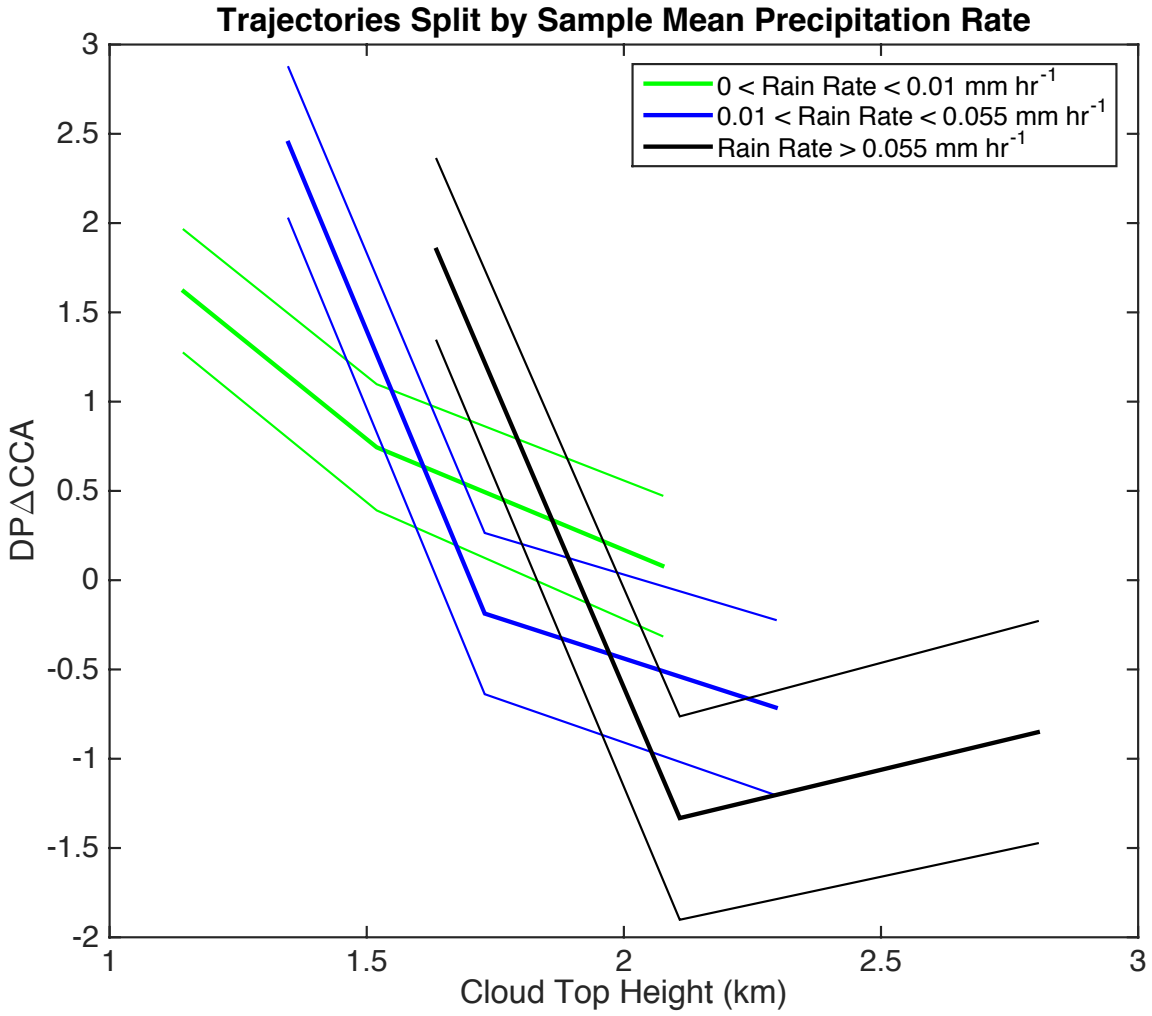

Figure 12. DP-Δ cloud cover anomalies for bins of constant cloud top height/PBL depth. Trajectories are divided into three groups based on the sample-mean rain rate at the beginning of the trajectory: Below median rain rate (green), 'moderate' rain rate (blue), and 'heavy' rain rate (black). Thick lines are the mean DP-Δ cloud cover anomalies, thin lines show the standard error (1-σ) of the mean. Bins are not uniform, but are instead chosen to have equal numbers of trajectories per bin, with 33% of the trajectories in each bin.